Front. Optoelectron. 2021, 14(4): 459–472
https://doi.org/10.1007/s12200-021-1133-4

REVIEW ARTICLE

Self-trapped exciton emission in inorganic copper(I) metal halides

Boyu ZHANG*, Xian WU*, Shuxing ZHOU, Guijie LIANG, Qingsong HU (✉)

Hubei Key Laboratory of Low Dimensional Optoelectronic Materials and Devices, Hubei University of Arts and Science, Xiangyang 441053, China

Abstract The broad emission and high photoluminescence quantum yield of self-trapped exciton (STE) radiative recombination emitters make them an ideal solution for single-substrate, white, solid-state lighting sources. Unlike impurities and defects in semiconductors, the formation of STEs requires a lattice distortion, along with strong electron–phonon coupling, in low electron-dimensional materials. The photoluminescence of inorganic copper(I) metal halides with low electron-dimensionality has been found to be the result of STEs. These materials were of significant interest because of their lead-free, all-inorganic structures, and high luminous efficiencies. In this paper, we summarize the luminescence characteristics of zero- and one-dimensional inorganic copper(I) metal halides with STEs to provide an overview of future research opportunities.

Keywords self-trapped exciton (STE), low electron-dimensional, inorganic copper(I) metal halides

1 Introduction

Halide perovskites have been recognized as a promising semiconductor material for next-generation optoelectronics, benefiting from high photoluminescence quantum yield (PLQY), tunable emission, and good charge mobility [1,2]. Photoelectric devices based on these materials, such as solar cells, light emitting devices, photodetectors, and lasers, have made unprecedented progress [2]. However, the long-term stability and toxicity of lead are major challenges to their commercialization [2]. To solve these problems, the strategy of replacing toxic lead with non-toxic ions (such as tin, germanium, antimony, and bismuth) has been extensively developed to maintain the advantageous properties of lead perovskites while improving the stability and reducing the toxicity [3–7]. However, some disadvantages still persist. Tin(II)-based perovskites have poor chemical stabilities, and Ge- or Bi-based metal halides have unsatisfactory photoelectric properties, which hamper their further optoelectronic applications [3,6,7].

Luo et al. reported a lead-free double perovskite, $Cs_2Ag(Na)In(Bi)Cl_6$, which is an important breakthrough [8]. This perovskite provides highly efficient and stable white light emission from self-trapped excitons (STEs). STEs are usually formed in semiconductors with low electron-dimensions and soft lattices [8]. Low electron-dimensionality is conducive to the carriers' localization, and the soft lattice can elastically deform under photoexcitation, which leads to strong electron–phonon coupling [9]. STEs have a large exciton binding energy [9], which is one of their remarkable characteristics. Ordinary exciton luminescence has slightly lower energy than the bandgap, but as an unconventional exciton, STEs have much smaller emission energies than the bandgap [10], because the emission energy of STEs is equal to the difference between bandgap energy and the exciton binding energy, self-trapping energy, and lattice deformation energy, which leads to the large Stokes shift of the STEs emission energy [10].

STEs are found widely in halide crystals, condensed rare gases, and organic molecular crystals [11]. Since the discovery of STE emission in inorganic copper(I)-based metal halides (Cu(I)MHs), with Cu(I)-X (X = Cl, Br, I) polyhedra as the basic unit, further research of the STE emission from these materials has been rapidly developed [12–17]. After Jun et al. first synthesized single crystals of $Cs_3Cu_2I_5$ [12], the high PLQY (90%) and air stability of low electron-dimensional Cu(I)MHs immediately attracted great attention. Subsequently, reports regarding the regulation of the luminescence properties of such low electron-dimensional compounds by ion substitution have emerged. Through anion mixing, the emission of zero-dimensional (0D) $Cs_3Cu_2X_5$ (X = Cl, Br, I) can be

Received December 21, 2020; accepted February 2, 2021

E-mail: qshu@hust.edu.cn

*B. Zhang and X. Wu contributed equally to this work.

modulated to green light (in $Cs_3Cu_2Cl_5$) from blue light (in $Cs_3Cu_2I_5$), whereas the emission of the one-dimensional (1D) $CsCu_2X_3$ (X = Cl, Br, I) analog can be tuned from green to yellow [15,18,19]. However, the emission and PLQY of Cu(I)MHs show non-monotonic changes. The emission of 1D A_2CuX_3 (A = Rb, K; X = Br, Cl) is mainly concentrated in the ultraviolet region with a small tuning range [13,16,20]. The compound $Cs_5Cu_3Cl_6I_2$, another 1D Cu(I)MH, produces pure blue light [21]. By changing the anions and cations in the material, the bandgap, exciton binding energy, self-trapping energy, and lattice deformation energy are changed, resulting in the modulation of the emission color, Stokes shift, full width at half maximum (FWHM), luminescence lifetime, and other properties. In addition to color modulation, unusual luminescence phenomena including pressure-induced luminescence enhancement, polarization-dependent PL emission, and multi-photon absorption have also been observed [22–24].

In this paper, we have summarized the current progress of inorganic Cu(I)MHs with STEs emission. The basic characteristics of STEs and their emission in these materials are described. The photophysical properties of STEs are explored from the perspective of the materials' crystal structures, spectral properties, and electronic structures. We introduce the applications of these materials in optoelectronic devices. Consequently, we discuss the challenges faced in the future use of all-inorganic Cu(I)MHs.

2 STEs in 0D inorganic Cu(I)MH materials

Jun et al. reported the novel lead-free 0D luminescent material $Cs_3Cu_2I_5$, which has a PLQY of nearly 90% for its single crystal and 60% for its thin film [12]. They attributed the emission to an excited-state structural reorganization mechanism caused by the Jahn–Teller distortion of tetrahedral Cu [12]. The inorganic and lead-free nature and efficient emission characteristics of $Cs_3Cu_2I_5$ attracted great attention. As a typical 0D inorganic Cu(I)MH, $Cs_3Cu_2X_5$ (X = Cl, Br, I) crystallizes in the orthorhombic structure with a Pnma space group. In this structure, a trigonal planar CuX_3 shares an edge with a tetrahedral CuX_4 unit to constitute a $[Cu_2X_5]^{3-}$ cluster. The $[Cu_2X_5]^{3-}$ dimers are completely separated by Cs^+ cations, as shown in Fig. 1(a).

Sebastia-Luna et al. suggested that Cu(I)MHs can form a continuous solid solution by exchanging the halogen from Cl^- to Br^- and Br^- to I^- [18]. Their XRD patterns are fitted using a Pnma space group. The unit cell parameters increase with increasing anion radius ($Cl^- < Br^- < I^-$) (Fig. 1(b)) [18]. Correspondingly, the emission shifts to higher energy overall; however, the shift in maximum excitation and emission wavelengths are not monotonic when increasing the halide ionic radius (from Cl^- to I^-) as shown in Fig. 1(c), which is in agreement with the PL characteristics of $Cs_3Cu_2Br_{5-n}I_n$ ($0 \leqslant n \leqslant 5$) reported in Refs. [15,18]. In general, the semiconductor bandgap decreases and the inter-band emission shifts to lower energy with increasing halogen anion radius. The emission shift trend here is different from that of inter-band radiation recombination, but analogous to that of CuX (X = Cl, Br, I) where the emission results from strong exciton-phonon coupling [15]. On the contrary, $Cs_3Cu_2X_5$ shows very large Stokes shifts, as shown in Table 1. Typically, PL spectra with such large Stokes shifts are attributed to STEs as a result of strong exciton-phonon coupling [15]. To verify this inference, the excitation power dependences of the PL for $Cs_3Cu_2X_5$ (X = Cl, Br, I) were measured [15,26,27]. As shown in Figs. 1(e)–1(g), the linear relationship between the emission intensity and the excitation power indicates the absence of permanent defects; hence, the emission likely originates from STEs [26]. There are some other effective experimental techniques to detect STE, such as characterizing the coupling strength of excitons and phonons, photoconversion spectroscopy [30]. Additionally, the broad excited-state transient absorption plateau across the probe region is a direct evidence of the formation of STEs [27]. Sebastia-Luna et al. suggested that the emission shift with the change of components may be caused by either halide segregation or phase segregation [18]. The XRD pattern of $Cs_3Cu_2Cl_5$ is better fitted using the space group Cmcm. Compared to other $Cs_3Cu_2X_5$ materials, $Cs_3Cu_2Cl_5$ has a significantly red-shifted PL (516 nm) because of the different crystal structure. The dual excitation and emission properties of $Cs_3Cu_2(Cl_{0.75}Br_{0.25})_5$ suggest the coexistence of the Cmcm phase (as $Cs_3Cu_2Cl_5$) and Pnma phase (as $Cs_3Cu_2Br_5$) [18].

To obtain further information about the emission mechanism, the temperature-dependent steady and transient state PLs of $Cs_3Cu_2Cl_5$ were measured over the range 300–20 K [26]. The results showed that the FWHM decreases gradually, the PL intensity increases, and the emission redshifts as the temperature decreases. The lack of free excitons emission with the change in temperature indicated that the self-trapped barrier is low and the photogenerated excitons are easily trapped [26]. The PL lifetimes of $Cs_3Cu_2Cl_5$ increased significantly from 112.4 μs at 300 K to 877.7 μs at 20 K, while the mono-exponential decay was maintained. The mono-exponentiality of the lifetime indicates that there is no change in the radiative and nonradiative channels [26]. This temperature-dependent PL characterization is essential for the analysis of the relevant mechanism. It is commonly used to calculate the exciton binding energy and the *S* factor associated with the electro-phonon coupling strength [10]. The formation of STEs usually requires materials with large exciton binding energies and *S* values. A large *S* value means that there is strong electro-phonon coupling [10].

Theoretical calculations found that the valence and

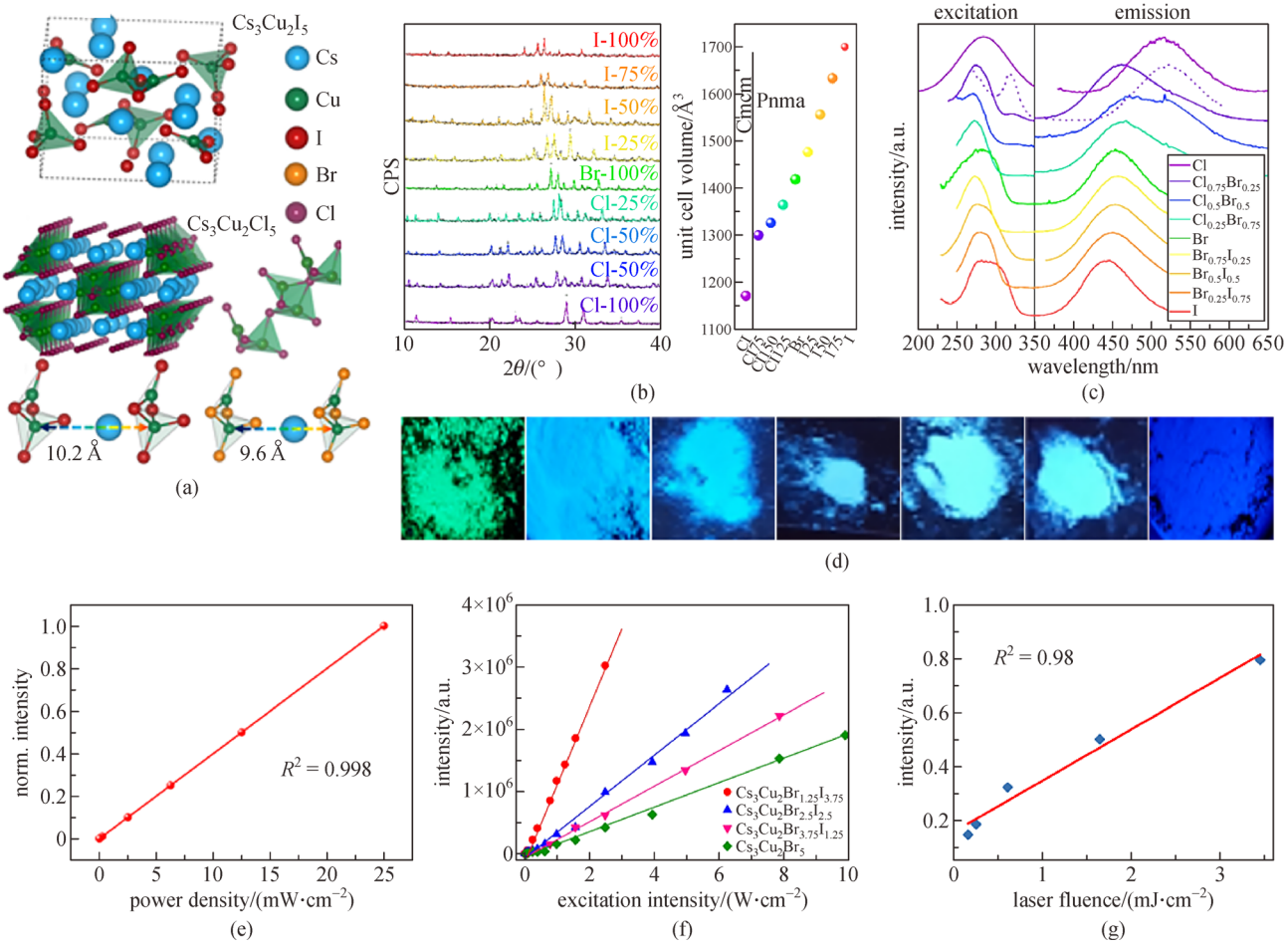

Fig. 1 (a) Crystal structure of $Cs_3Cu_2I_5$ (top), and $Cs_3Cu_2Cl_5$ (middle). Two adjacent copper halide polyhedra (bottom) of $Cs_3Cu_2I_5$ (left) and $Cs_3Cu_2Br_5$ (right) along one of the crystal directions [25]. (b) X-ray diffraction (XRD) (left) and unit cell volumes (right) of different $Cs_3Cu_2X_5$ (X = Cl, Br, I) compounds [18]. (c) PLE (left) and PL (right) spectra of different $Cs_3Cu_2X_5$ [18]. (d) Images of the powders of different $Cs_3Cu_2X_5$ (X = Cl, Br, I) compounds under ultraviolet irradiation [15,26]. (e) Integrated PL intensity vs. excitation power for $Cs_3Cu_2Cl_5$ [26]. (f) Integrated PL intensity vs. excitation power for $Cs_3Cu_2Br_{5-n}I_n$ (n = 0, 1.25, 2.50, 3.75) [15]. (g) Integrated PL intensity vs. excitation power for $Cs_3Cu_2I_5$ [27]

conduction bands of $Cs_3Cu_2X_5$ (X = Cl, Br, I) are mainly consist of Cu 3d and Cu 4s states (Figs. 2(a)–2(c)), indicating that they have narrow bandgaps [15,26]. Roccanova et al. suggests that the structural distortion breaks the two Cu–halogen bonds and moves the two Cu atoms closer to each other in the $[Cu_2X_5]^{3-}$ cluster, as shown in Fig. 2(d) [15]. The hole has Cu 3d character and is localized on the two Cu atoms in the $[Cu_2X_5]^{3-}$ cluster, whereas the electron is localized mostly in the bond-center position between the two Cu atoms [15]. The spatial distribution of the electron and hole of the exciton in $Cs_3Cu_2I_5$ is similar to that in $Cs_3Cu_2Br_5$ [15]. Lian et al. suggested that the photoexcitation induces a local structural distortion of $Cs_3Cu_2X_5$ (X = Cl, Br, I), and the $[Cu_2X_5]^{3-}$ cluster is converted into a spindle-like species (two tetrahedrons sharing a face), decreasing the Cu-Cu distance as illustrated in Fig. 2(e) [26]. The distortion enhanced the local symmetry of the spindle-like $[Cu_2X_5]^{3-}$ and decreased the energy barrier for the formation of STEs, which explains the origin of the single emission from the STEs in $Cs_3Cu_2X_5$ (X = Cl, Br, I) [26]. In this situation, the valence band maximum (VBM) shows stronger charge localization. However, as the anion goes down the halogen group, the increase of anionic p-component mixing with the Cu 3d orbitals leads to weakening of the VBM. This result partially explains the abnormal blue-shift in the emission of $Cs_3Cu_2X_5$ (X = Cl, Br, I) when the anion changes from Cl^- to Br^- to I^- [26]. The calculations of Zhang et al. reveal that the electron and hole are separated spatially. This spatial separation impedes the recombination of the electron and hole and thus prolongs the PL lifetimes of $Cs_3Cu_2X_5$ (X = Cl, Br, I) [15,26]. Because of the highly localized electron and hole, the emission of $Cs_3Cu_2Cl_5$ is insensitive to defects, giving rise to the high PLQY and the mono-exponential PL decays.

Table 1 PLE, PL, lifetime (τ), PLQY, bandgap (E_g), FWHM, and Stokes shift (ΔS) of $Cs_3Cu_2X_5$ (X = Cl, Br, I) reported in the literatures

material	PLE/nm	PL/nm	τ/μs	PLQY/%	E_g/eV	FWHM/nm	ΔS/nm	Ref.
$Cs_3Cu_2Cl_5$	259	527	135.97	48.7	4.43	–	242	[17]
$Cs_3Cu_2Cl_5$	~283	516	–	78.0	–	–	~235	[18]
$Cs_3Cu_2Cl_5$	310	525	–	60.0	–	102	215	[25]
$Cs_3Cu_2Cl_5$	320	515	112.4	91.3	3.60	91	195	[26]
$Cs_3Cu_2(Cl_{0.75}Br_{0.25})_5$	~275	516	–	10.0	–	–	~185	[18]
$Cs_3Cu_2(Cl_{0.5}Br_{0.5})_5$	~272	470	–	3.6	–	–	~195	[18]
$Cs_3Cu_2(Cl_{0.25}Br_{0.75})_5$	~273	464	–	3.3	–	–	~190	[18]
$Cs_3Cu_2Br_5$	298	455	–	50.1	4.51	75	157	[15]
$Cs_3Cu_2Br_5$	269	461	14.12	16.9	4.33	–	–	[17]
$Cs_3Cu_2Br_5$	293	460	–	10.0	–	73	167	[25]
$Cs_3Cu_2Br_5$	290	461	–	17.3	3.72	82	171	[26]
$Cs_3Cu_2Br_{3.75}I_{1.25}$	293	456	–	53.8	–	85	164	[15]
$Cs_3Cu_2Br_{2.5}I_{2.5}$	294	453	–	55.2	–	89	159	[15]
$Cs_3Cu_2Br_{1.25}I_{3.75}$	300	448	–	60.4	–	93	148	[15]
$Cs_3Cu_2I_5$	290	445	–	91.2	–	175	155	[12]
$Cs_3Cu_2I_5$	309	443	–	98.7	–	99	135	[15]
$Cs_3Cu_2I_5$	262, 285	445	1.56	29.2	4.40	–	158	[17]
$Cs_3Cu_2I_5$	310	440	–	62.0	–	80	130	[25]
$Cs_3Cu_2I_5$	305	445	–	49.2	4.06	77	140	[26]
$Cs_3Cu_2I_5$	286	444	1.12	–	4.10	79	–	[28]
$Cs_3Cu_2I_5$	316	437	–	95.0	–	–	–	[29]

3 STE in 1D inorganic Cu(I)MH materials

Three typical crystal structures of 1D Cu(I)MH are shown in Figs. 3(a)–3(f). Specifically, $CsCu_2X_3$ (X = Cl, Br, I) belongs to the orthorhombic Cmcm space group, where CuX_4 tetrahedra share common edges, forming 1D chains separated by Cs^+ ions [18]. Furthermore, A_2CuX_3 (A = Rb, K; X = Br, Cl) crystallizes in an orthorhombic structure with a Pnma space group, where CuX_4 tetrahedra share a common corner, forming 1D chains separated by A^+ ions along the b-axis [20]. The mixed halide compound $Cs_5Cu_3Cl_6I_2$ belongs to the orthorhombic Cmcm space group, where the alternately connected $[CuCl_2I_2]_2$ unit and a single $[CuCl_2I_2]$ unit form 1D zigzag chains of $[Cu_3Cl_6I_2]_n^{5n-}$, where only I^- ions bridge between these units as shown in Fig. 3(e). Similar to $CsCu_2X_3$, the 1D $[Cu_3Cl_6I_2]_n^{5n-}$ chains were separated by Cs^+ ions [21].

In contrast to the blue-shift of the $Cs_3Cu_2X_5$ (X = Cl, Br, I) emission with increasing anion radius, the emission of the single halide in $CsCu_2X_3$ (X = Cl, Br, I) shows a continuous red-shift with an increase in the Stokes shift [19]. However, the emission shifts of the mixed halides $CsCu_2Cl_{1.5}Br_{1.5}$ and $CsCu_2Br_{1.5}I_{1.5}$ do not follow a linear trend, and their maximum emission is red-shifted with lower PL efficiency compared to that of the single halide compounds (Table 2) [19]. Exceptionally, mixed Br–Cl compounds, which are rich in Cl^-, demonstrate minor phase segregation between $CsCu_2Br_3$ and $CsCu_2Cl_3$ [19]. For mixed halides, the emission behaviors are similar to those observed for $MAPb(IBr)_3$ [19]. These facts could be explained by the presence of greater structural distortion in the mixed halide samples, which can affect the PL efficiency as well as the self-trapped depth within the bandgap of the material and result in a red-shift of the PL maximum [19]. Particularly, the PL lifetimes of $CsCu_2X_3$ (X = Cl, Br, I) increase from 13.8 ns for $CsCu_2Cl_3$ to 62 ns for $CsCu_2I_3$, following the trend opposite to the PL lifetimes of $Cs_3Cu_2X_5$ (X = Cl, Br, I). The PL lifetimes of $CsCu_2X_3$ (X = Cl, Br, I) are also one to two orders of magnitude shorter than those of $Cs_3Cu_2X_5$ (X = Cl, Br, I) [19,26]. The temperature-dependent PL shows that the emission of $CsCu_2I_3$ is continuously blue-shifted with increasing temperature [14]. A similar blue-shift was also observed in almost all $CsCu_2X_3$ (X = Cl, Br, I) compounds [19]. As mentioned above, such an abnormal blue-shift phenomenon is caused by the high lattice distortion and the electron–phonon renormalization.

To better understand STE emission in non-octahedral units, Li et al. investigated the pressure-induced PL enhancement in 1D Cu(I)MH $CsCu_2I_3$ [22]. The experimental results show that the slight structural distortion of

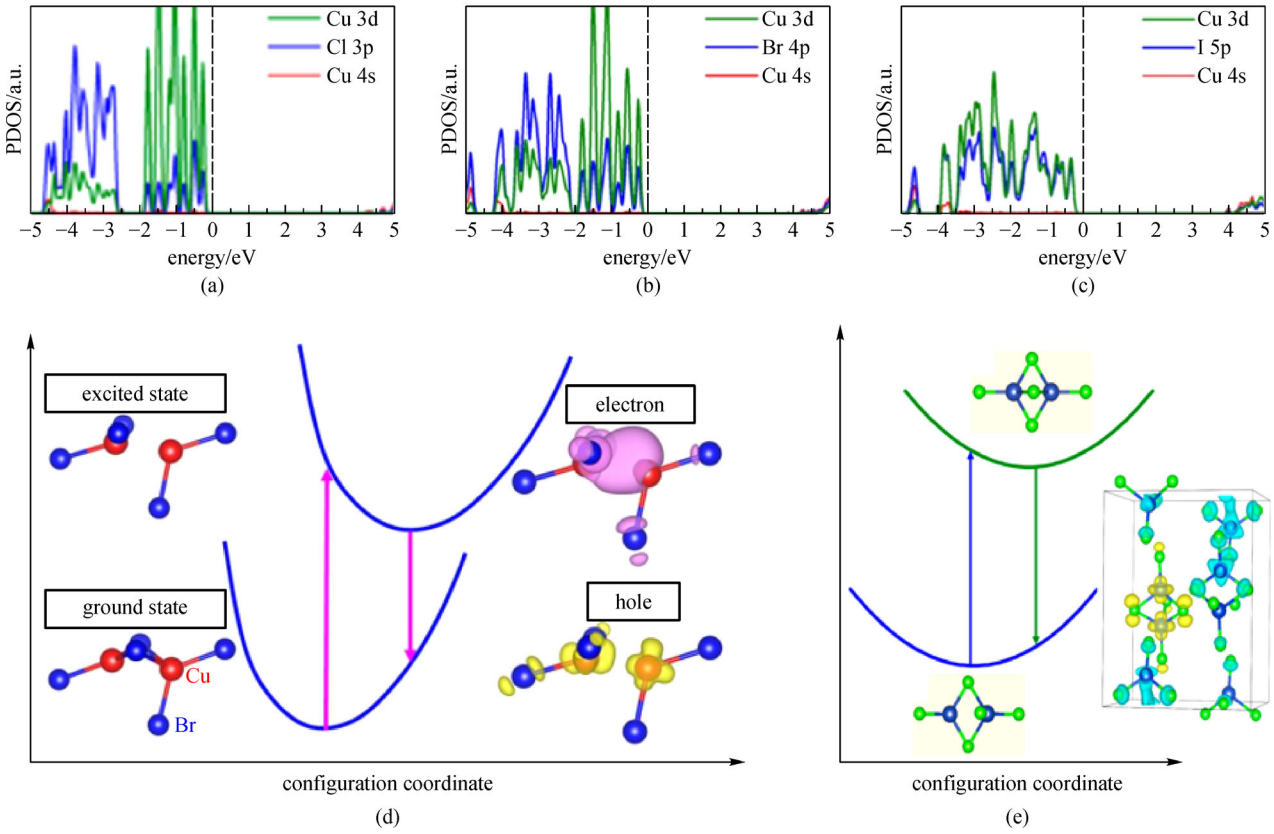

Fig. 2 Projected density states for pristine structures of (a) $Cs_3Cu_2Cl_5$, (b) $Cs_3Cu_2Br_5$, and (c) $Cs_3Cu_2I_5$ [26]. (d) Configuration coordinate diagram for the excitation, relaxation, and emission in $Cs_3Cu_2Br_5$ [15]. (e) Configuration coordinate diagram for the formation of STEs in $Cs_3Cu_2Cl_5$ [26]

the $CuCl_4$ tetrahedra leads to bandgap broadening and STE enhancement under mild compression from 1 atm to 4.1 GPa. Such changes result in the increase of emission energy and intensity for $CsCu_2I_3$ in phase I. Meanwhile, the slight structural distortion results in a lower detrapping barrier, weaker electron–phonon coupling strength, and lower activation energy [22]. Therefore, the STE emission efficiencies of phase I are relatively low under this mild compression. The emission intensity is significantly enhanced with further continuous compression to 8.0 GPa. However, it is quenched with further compression beyond this limit, because the strong structural distortions lead to a phase transition and greatly increase the electron–phonon coupling, inducing a higher detrapping barrier and larger activation energy [22]. Thus, less STEs can be detrapped from the ST state to the free exciton (FE) state in phase II (Fig. 3(i)). This relatively increases the concentration of STEs, thus enhancing the STE emission [32,33]. The emission quenching phenomenon at high compression is usually attributed to the synergistic effect of deviatoric stress and structural amorphization [34].

The electronic structures of 1D Cu(I)MH materials are similar to the 0D Cu(I)MH mentioned above. The valence band (VB) and conduction band (CB) are predominantly composed of Cu 3d orbital and mixed Cu 4s orbitals. The M^+ (Cs^+, Rb^+, K^+, etc.) ions are far away from the VB and CB, so their contribution to the energy band can be ignored [13,15,16,20,26]. In addition, the electronic structures of Cu(I)MHs significantly change upon photoexcitation, which is strongly correlated with their optical properties [26]. Du also found, using first principles calculations, that the emission energy of $CsCu_2Cl_3$, $CsCu_2Br_3$, and $CsCu_2I_3$ STEs decreased gradually as the anion goes down the halogen group [35]. The red-shift trend experimentally observed for the emission spectra of the three materials is not caused by the electronegativity of anions, but rather from the different STE properties [35]. Du's calculation showed that each $CsCu_2X_3$ (X = Cl, Br, I) has three different STE states. Figure 4(a) shows the partial charge density contours of both the hole and electron wave functions for STE1 and STE2 in $CsCu_2Cl_3$ and STE3 in $CsCu_2I_3$. The calculated emission of $CsCu_2Br_3$ and $CsCu_2I_3$ originates from the irradiative transfer of the lowest energy level of the STE, whereas $CsCu_2Cl_3$ emits from the STE's metastable energy level [35]. These results are in excellent agreement with the experimental results. Based on Du's calculations, Kentsch et al. suggest that the exciton self-trapped process in $CsCu_2I_3$ films was directly

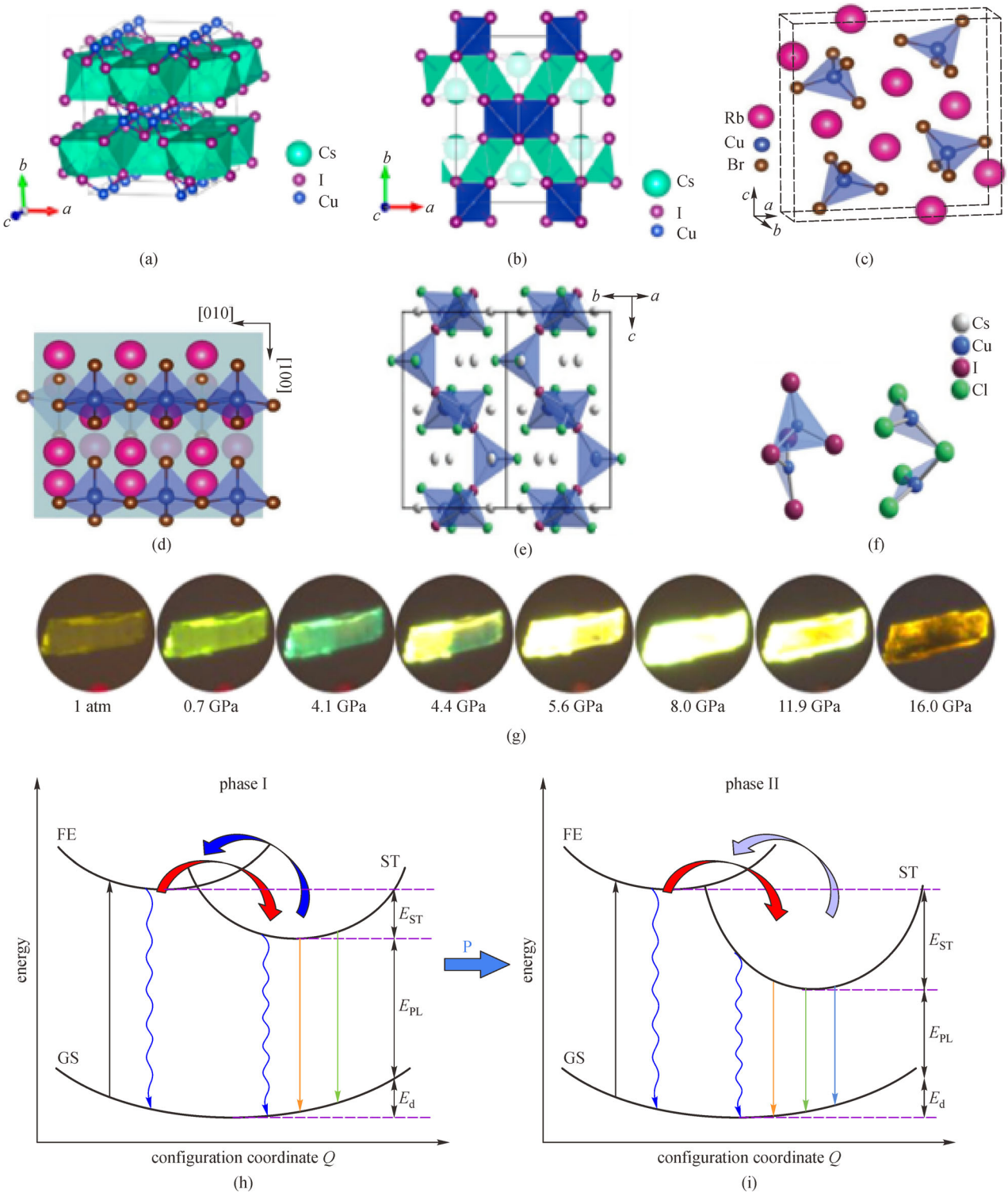

Fig. 3 (a) Crystal structure of $CsCu_2I_3$ [31]. (b) $CsCu_2I_3$ structure viewed along the *c*-axis [31]. (c) Crystal structure of Rb_2CuBr_3 [20]. (d) Rb_2CuBr_3 structure viewed along the *a*-axis [20]. (e) Crystal structure of $Cs_5Cu_3Cl_6I_2$ [21]. (f) $[Cu_2I_5]^{3-}$ unit in $Cs_5Cu_3Cl_6I_2$ (Pnma) (left) and the $[Cu_2Cl_5]^{3-}$ unit in $Cs_5Cu_3Cl_6I_2$ (Cmcm) (right) [21]. (g) PL micrographs of $CsCu_2I_3$ crystal under pressures from 1 atm up to 16.0 GPa [22]. Schematic illustrations of the trapping and detrapping processes of the excitons in (h) phase I and (i) phase II. FE, free exciton state; GS, ground state; ST, self-trapped state; E_{ST}, self-trapping energy; E_{PL}, photoluminescence energy; E_d, lattice deformation energy [22]

Table 2 PLE, PL, τ, PLQY, E_g, FWHM, and ΔS of $CsCu_2X_3$ (X = Cl, Br, I), A_2CuX_3 (A = Rb, K; X = Br, Cl), and $Cs_5Cu_3Cl_6I_2$ from the literatures

material	PLE/nm	PL/nm	τ/μs	PLQY/%	E_g/eV	FWHM/nm	ΔS/nm	Ref.
$CsCu_2Cl_3$	319	527	0.0138	48.0	4.29	102	208	[19]
$CsCu_2Cl_{1.5}Br_{1.5}$	340	587	0.0151	0.37	–	200	247	[19]
$CsCu_2Br_3$	319	533	0.018	18.3	3.94	106	214	[19]
$CsCu_2Br_{1.5}I_{1.5}$	335	584	0.0266	0.38	–	128	249	[19]
$CsCu_2I_3$	347	568	0.0636	15.7	3.78	75	245	[14]
$CsCu_2I_3$	331	575	–	6	–	120	244	[25]
$CsCu_2I_3$	321	561	0.104	–	3.6	–	–	[28]
$CsCu_2I_3$	334	576	0.062	3.23	3.93	126	242	[19]
Rb_2CuCl_3	300	395	12.21	85	4.49	52	93	[13]
Rb_2CuBr_3	276	385	41.4	64	3.51	54	85	[13]
Rb_2CuBr_3	300	385	41.4	98.6	3.51	54	85	[20]
Rb_2CuBr_3	302	390	–	20	–	54	88	[25]
K_2CuCl_3	291	392	–	96.58	–	54	101	[16]
K_2CuBr_3	296	388	–	55	–	54	92	[16]
$Cs_5Cu_3Cl_6I_2$	–	462	40	95	–	95	191	[21]

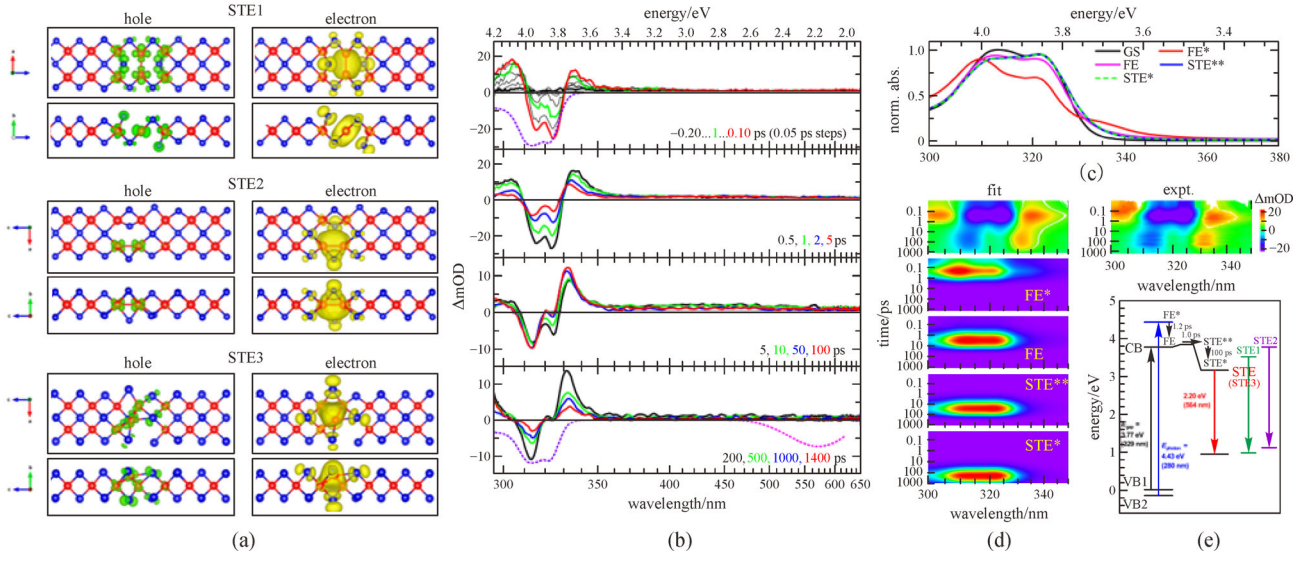

Fig. 4 (a) Partial charge density contours of both hole and electron wave functions for STE1 and STE2 in $CsCu_2Cl_3$ and STE3 in $CsCu_2I_3$, viewed from the two directions (along the *b* and *a* axes, respectively) perpendicular to the 1D chain [35]. (b) Femtosecond UV–vis transient absorption broadband spectra of a $CsCu_2I_3$ thin film [36]. Each curve in the figure represents the absorption curve of the $CsCu_2I_3$ film at a certain moment, and the vertical axis represents the change of absorption at a certain moment compared to the time zero. (c) Species-associated spectra were obtained from the kinetic modeling. Species: FE* and FE (hot and cooled free excitons, respectively), STE** and STE* (hot and partially cooled STEs, respectively). GS is the "ground-state" absorption (black solid line) [36]. (d) Semilogarithmic contour plots of experimental transient absorption spectra (right) and fitted transient absorption spectra (left), the latter with additional representations of the spectral evolution for each species [36]. (e) Energy level scheme summarizing the states, transitions, and central dynamic processes in $CsCu_2I_3$ thin films. Energetics of STE1, STE2, and STE3 are taken from Refs. [35,36]

observed by femtosecond transient absorption [36]. The edge absorption bimodal structure is derived from the 130 meV spin orbital splitting of the Cu d electrons. The formation of the lowest level of the STE state results in the disappearance of band edge absorption. The experiment showed that the time constant of the self-trapped process of the thermal relaxation free exciton is 12 ps and the energy barrier is not lower than 60 meV [36]. Each process is obtained by species-associated spectra synthesis. It is probably the most powerful experimental description of STE at present.

The emission from $CsCu_2X_3$ (X = Cl, Br, I) has a large

FWHM and Stokes shift, similar to the above-mentioned characteristics of the STEs in $Cs_3Cu_2X_5$ (X = Cl, Br, I), but it exhibits the shorter PL lifetime. It is unusual that although a STE mechanism is observed, the FWHM and Stokes shift of the A_2CuX_3 (A = Rb, K; X = Cl, Br) emission are much smaller than those of $CsCu_2X_3$ (X = Cl, Br, I). In addition, Rb_2CuCl_3 showed an upconversion emission phenomenon [13]. In this process, photons with lower energy than the bandgap interact with the lattice, causing absorption of phonons in the lattice and subsequent emission of photons with higher energy than before. This mechanism leads to the extraction of heat energy from the lattice to emit the higher energy photon, which cools down the material. The advantages of high PLQY and low trapped state density in these Cu(I)MHs are important parameters for optical cooling [13]. Among all the reported inorganic 1D Cu(I)MHs, $Cs_5Cu_3Cl_6I_2$ was the only one to emit pure blue emission, with a near-unity quantum yield of ≈95%. The flat valence bands promote the formation of localized holes, leading to STE formation. The photo-deformable nature of the copper halogen polyhedra facilitates highly efficient STEs, leading to efficient radiative recombination [21].

4 Applications of inorganic Cu(I)MH STE materials

Based on the advantages mentioned above, inorganic Cu(I)MH STE materials are very suitable for applications in lighting and displays as a phosphor. $Cs_3Cu_2I_5$ and $CsCu_2I_3$ (Fig. 5) can coexist in the synthesis process; this gives the opportunity to obtain tunable white light emission using a simple mechanochemical method to quickly synthesize mixed-phase materials with different proportions [37]. Fang et al. used this method to obtain white luminescent samples by mixing $CsCu_2I_3$ and $Cs_3Cu_2I_5$ with different ratios. When the mixture had a mass ratio of 8:3, the sample emitted with a Commission Internationale de L'Eclairage (CIE) chromaticity coordinate of (0.36, 0.36) [37]. In other reports, pure $CsCu_2I_3$ and $Cs_3Cu_2I_5$ materials (powders and nanocrystals) were synthesized first and then mixed in suitable proportions to produce white light emitters [25,28]. Furthermore, $CsCu_2I_3$ single crystal (SC) has great potential in energy-saving white lighting because of its bimodal emission [14,41]. However, ensuring the stability of the light efficiency and color at different temperatures is a key problem to be solved in the lighting and display applications of such materials.

Inorganic Cu(I)MH STE materials can also be directly used as an electroluminescent layer in LED devices. Ma et al. fabricated $CsCu_2I_3$-based LEDs with an ITO/PEDOT:PSS/poly-TPD/$CsCu_2I_3$/TPBi/LiF/Al structure [38]. The best device had a turn-on voltage of about 5.0 V, a maximum luminance (L_{max}) value of 47.5 cd/m^2 at an applied bias voltage of 9.2 V, and maximum external quantum efficiency (EQE) of 0.17% [38]. Then they constructed a high color-rendering index (CRI = 91.6) and stable white light-emitting diode (WLED) with an ITO/

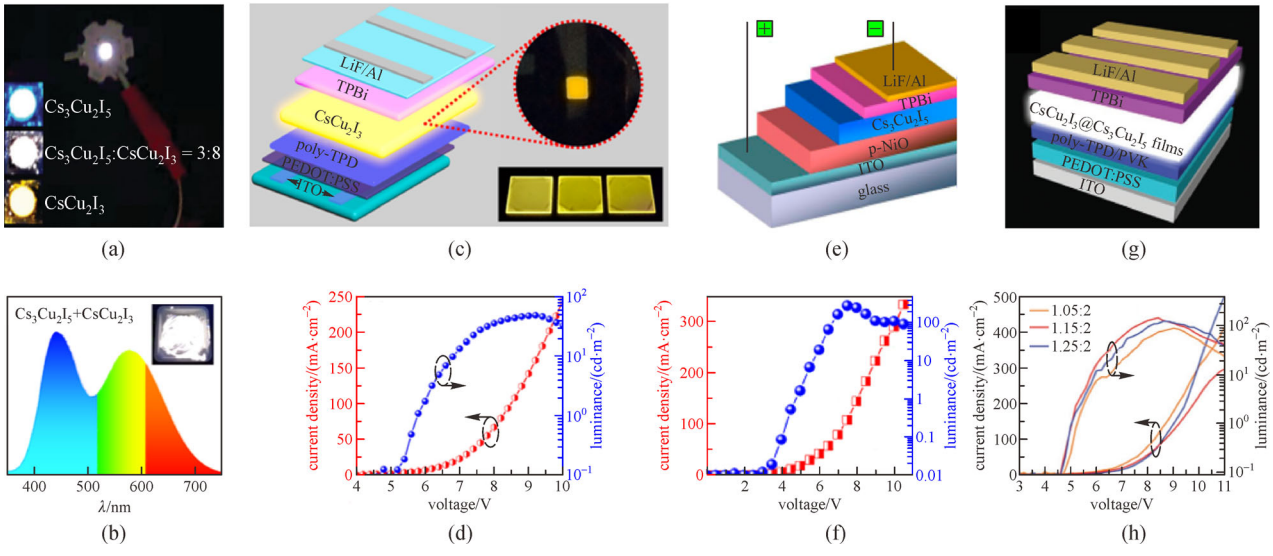

Fig. 5 (a) Photo of a white LED driven under a bias voltage of 6 V. The inset shows photographs of $Cs_3Cu_2I_5$, a $Cs_3Cu_2I_5$ + $CsCu_2I_3$ mixture, and $CsCu_2I_3$ (from top to bottom) under UV light irradiation at 305 nm [37]. (b) PL spectrum of the $Cs_3Cu_2I_5$ + $CsCu_2I_3$ mixture (with weight ratio of 1:16 or molar ratio of 1:8). Inset shows a photograph of the mixture under 254 nm light irradiation [25]. (c) Schematic structure of the $CsCu_2I_3$ based-LEDs [38]. (d) Voltage–current density–luminance curves of the yellow emission LEDs [38]. (e) Schematic structure of the $Cs_3Cu_2I_5$ NCs-based LEDs [39]. (f) Voltage–current density–luminance curves of the blue emission device [39]. (g) Schematic structure of the $CsCu_2I_3$@$Cs_3Cu_2I_5$-based LEDs [40]. (h) Voltage–current density–luminance curves of the white emission device [40]

PEDOT:PSS/poly-TPD/PVK/$CsCu_2I_3$@$Cs_3Cu_2I_5$/TPBi/LiF/Al structure [40]. Liu et al. also reported a WLED with an ITO/PEDOT:PSS/V-NPB/$CsCu_2I_3$@$Cs_3Cu_2I_5$/SPPO13/LiF/Al structure. This WLED had a CIE chromaticity coordinate of (0.327, 0.348) and a CRI of up to 94 [29]. Wang et al. reported deep-blue LEDs using $Cs_3Cu_2I_5$ nanocrystals as the electroluminescent layer [39]. These blue LEDs had a glass/ITO/p-NiO/$Cs_3Cu_2I_5$/TPBi/LiF/A structure, a turn-on voltage of about 4.5 V, a L_{max} value of 262.6 cd/m^2 at 7.5 V, and an EQE of ~1.12% at an applied bias voltage of 7.5 V [39]. These results indicated that copper(I) halides are promising as an environment-friendly and stable emitter for LEDs and are compatible with the practical applications of the devices.

Photodetection is another important application of these high-efficiency inorganic Cu(I)MH STE materials. Li et al. reported $Cs_3Cu_2I_5$-based ultraviolet photodetectors with high spectral selectivity [42]. The $Cs_3Cu_2I_5$/GaN heterojunction device had a narrow spectral response "window" of 300–370 nm, and the response range can be adjusted by changing the thickness of $Cs_3Cu_2I_5$ film and bias voltage [42]. At zero bias, the responsivity, detection rate, maximum current on/off ratio, and response speeds were 0.28 A/W, 1.4×10^{12} Jones, 1.2×10^5, and 95/130 μs, respectively [42]. These values are comparable to those of the numerous previously reported lead halide photodetectors [42]. In addition, Zhang et al. reported a $Cs_3Cu_2I_5$-based deep ultraviolet photodetector with a responsivity of 64.9 mA/W, a specific detectivity of 6.9×10^{11} Jones, a turn-on ratio of 127, and response speeds of 26.2/49.9 ms for the rise/fall time [43]. Li et al. also constructed a polarization-sensitive and flexible ultraviolet photodetector using 1D $CsCu_2I_3$ nanowires, which had a high photocurrent anisotropy ratio up to 3.16 because of the electrical and optical anisotropy of the asymmetric structure and the external morphological anisotropy [23]. The device had an on/off ratio of 2.6×10^3, a response speed of 6.94/214 μs, a photoresponsivity of 32.3 A/W, and a specific detectivity of 1.89×10^{12} Jones [23]. Similarly, Yang et al. fabricated a deep ultraviolet photodetector based on a $CsCu_2I_3$ film [31]. The on/off ratio, responsivity, specific detectivity, and EQE of this device were 22, 22.1 mA/W, 1.2×10^{11} Jones, and 10.3%, respectively, under 265 nm illumination with a light density of 0.305 mW/cm^2 [31]. Furthermore, Fang et al. observed the facet-dependent photoresponse of a $CsCu_2I_3$ single crystal, whose morphology consists of 010, 110, and 021 crystal planes (Fig. 6) [44]. The lower dark current of the 010 crystal plane results in the on-off ratio being higher than that of 110 crystal plane [44]. This work gives new insights into the 1D electronic structure associated with high anisotropy.

Other possible applications of inorganic Cu(I)MH STE materials have also been explored, such as X-ray scintillators, fluorescent inks, image sensors, and memristors and neuromorphic computing applications [20,43,45–49]. The excellent luminescence performance and lack of self-absorption in $RbCu_2Br_3$, $RbCu_2Cl_3$, K_2CuBr_3, and $Cs_3Cu_2I_5$ led to a good scintillation response to X-ray signals, with a high light yield of 91056, 16600, 23806, and 79279 photons per meV, respectively [20,45–47]. Zhang et al. reported a fluorescent ink developed from a $Cs_3Cu_2I_5$/polyvinylidene fluoride precursor solution. This work showed potential applications of $Cs_3Cu_2I_5$ for anti-counterfeiting and encryption fields (Fig. 7) [48]. Zhang et al. explored the image-sensing capability of $Cs_3Cu_2I_5$ crystalline films, where purple and light purple images can be readily formed under 265 and 365 nm illuminations, respectively [43]. Furthermore, Zeng et al. investigated the application of $Cs_3Cu_2I_5$ films in the field of memristors and neuromorphic computing [49]. Ag/PMMA/$Cs_3Cu_2I_5$/ITO structure memristors exhibited a bipolar resistive switching operating voltage lower than ±1 V, a large on/off ratio (up to 10^2), stable endurance over 100 cycles, and a retention time longer than 10^4 s [49].

5 Conclusions and perspective

We have summarized the recent progress made in the field of STE emission from inorganic Cu(I)MHs. Novel 0D and 1D inorganic Cu(I)MHs STE luminescent materials, such as $Cs_3Cu_2X_5$ (X = Cl, Br, I), $CsCu_2X_3$ (X = Cl, Br, I), A_2CuX_3 (A = Rb, K; X = Cl, Br), and $Cs_5Cu_3Cl_6I_2$, have been developed and researched. The basic features of STE luminescence have been summarized, methods for identifying STE luminescence have been proposed, and the application of these materials has been introduced. Evidently, the STE luminescence can be regulated by substituting cations and anions. In the process of ion modulation, the emission and light efficiency usually change non-monotonically, but the essential reason for this is currently unclear. Among the 1D materials, only $CsCu_2X_3$ has a PL lifetime of the order of nanoseconds, whereas other materials have a PL lifetimes of the order of microseconds. In addition, A_2CuX_3 (A = Rb, K; X = Cl, Br) have incomprehensible small emission FWHMs and Stokes shifts. These issues have not been thoroughly studied. Meanwhile, the formation process of STEs in this kind of material is rarely studied, and the direct experimental observation has not been realized. Therefore, the modulation mechanism has not been completely understood. A profound understanding of STE formation processes and modulation mechanisms is conducive to the accurate judgment and regulation of material properties and the development of similar materials with desired target properties. These studies will be essential for the performance optimization and extend the application of inorganic Cu(I)MH STEs and similar materials.

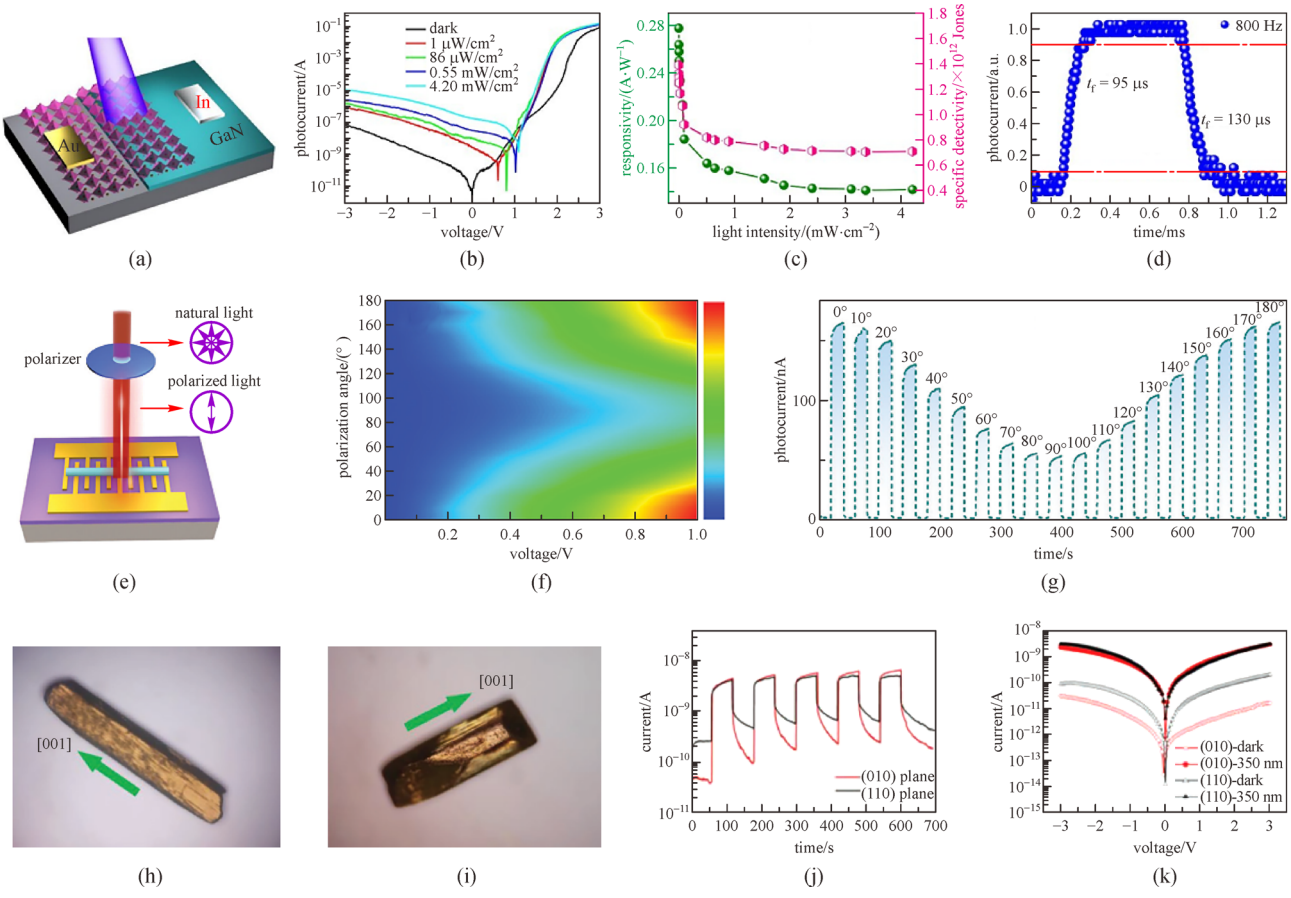

Fig. 6 (a) Schematic illustration of the $Cs_3Cu_2I_5$/GaN heterojunction device [42]. (b) *I*–*V* curves of the photodetector tested in the dark and under different light irradiation intensities (320 nm) [42]. (c) Responsivity and specific detectivity of the photodetector versus light intensity [42]. (d) Rising and falling edges for estimating the rise time (t_r) and fall time (t_f) of the photodetector [42]. (e) Schematic illustration of the polarization-sensitive photodetector based on 1D $CsCu_2I_3$ nanowires (NWs) [23]. (f) Anisotropic photocurrent response under 325 nm light excitation described via a 2D color map (photocurrent is denoted by the color bar, with voltage as the *x*-axis and polarization angle as the *y*-axis) [23]. (g) Photocurrent response of a 1D $CsCu_2I_3$ NW device under incident light with different polarization angles [23]. (h) and (i) Optical microscopy images of $CsCu_2I_3$ single crystals with rod-shaped morphology [44]. Comparison of photoelectric properties between (110) and (010) crystal planes of $CsCu_2I_3$ single crystals: (j) *I*–*t* curves and (k) *I*–*V* curves in dark and under 350 nm illumination at a 3 V bias [44]

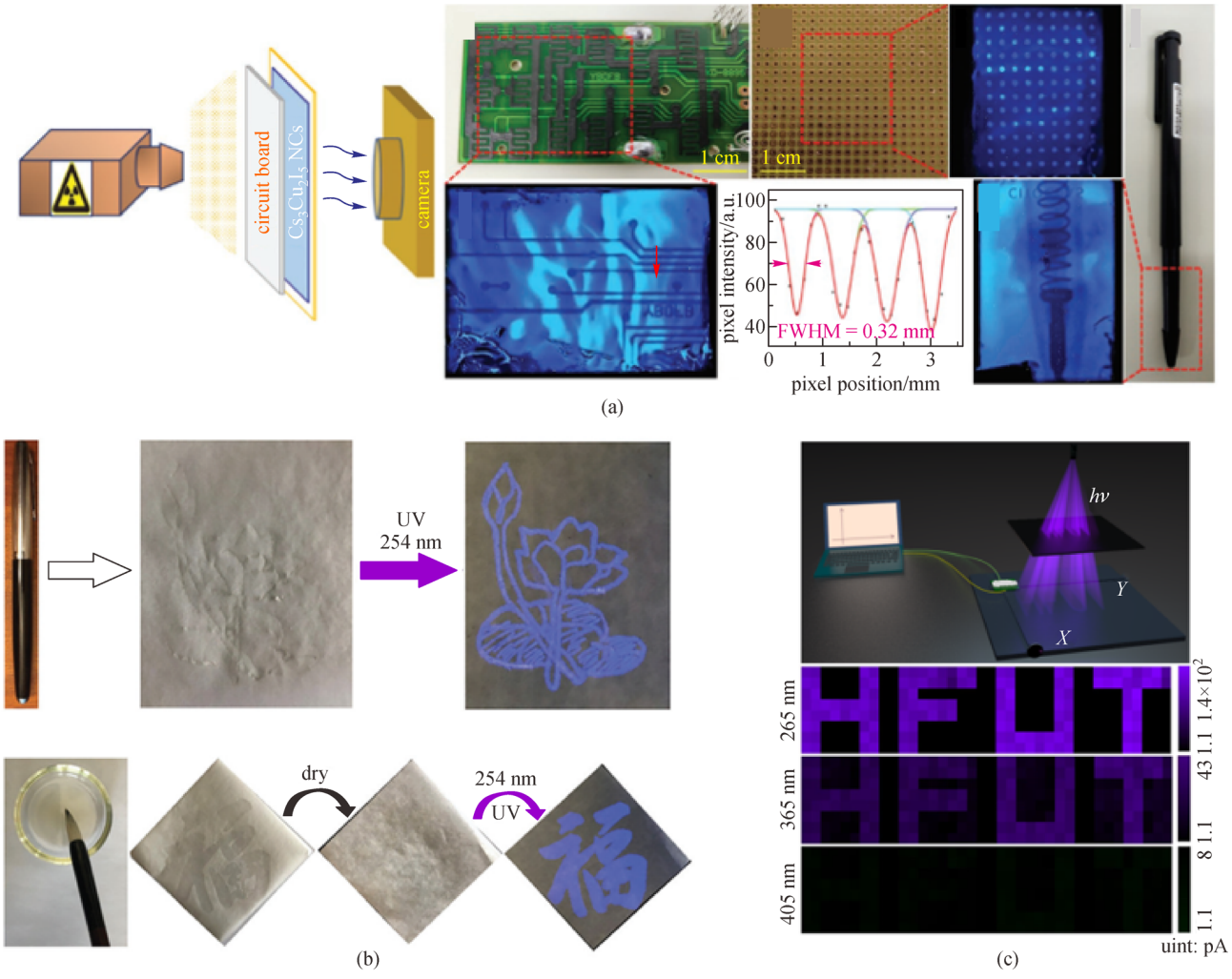

Fig. 7 (a) Schematic of the prototype projection system for X-ray imaging, and photographs of an X-ray image of a universal board and a ball-point pen [47]. (b) Illustration of $Cs_3Cu_2I_5$ precursor solution as a fluorescent ink [48]. (c) Schematic illustration of the setup for recording deep UV images and the image-sensing profile of HFUT under 265, 365, and 405 nm light excitation [43]

Acknowledgements Q. Hu acknowledges the support from the National Key Research and Development Plan of China (No. 2019YFE0107200), the National Natural Science Foundation of China (Grant No. 11705277), the Natural Science Foundation of Hubei Province (No. 2020CFB700), the Doctoral Research Foundation Project of Hubei University of Arts and Science (No. kyqdf2020023), and Innovation Research Team Project of Hubei University of Arts and Science (No. 2020kypytd001).

References

1. Guo Z, Li J, Pan R, Cheng J, Chen R, He T. All-inorganic copper(I)-based ternary metal halides: promising materials toward optoelectronics. Nanoscale, 2020, 12(29): 15560–15576
2. Tang J, Li D. Halide perovskites: from materials to optoelectronic devices. Frontiers of Optoelectronics, 2020, 13(3): 191–192
3. Wang L, Chen P, Kuttipillai P S, King I, Staples R, Sun K, Lunt R R. Epitaxial stabilization of tetragonal cesium tin iodide. ACS Applied Materials & Interfaces, 2019, 11(35): 32076–32083
4. Chen J, Luo Z, Fu Y, Wang X, Czech K J, Shen S, Guo L, Wright J C, Pan A, Jin S. Tin(IV)-tolerant vapor-phase growth and photophysical properties of aligned cesium tin halide perovskite ($CsSnX_3$; X = Br, I) nanowires. ACS Energy Letters, 2019, 4(5): 1045–1052
5. Wong A B, Bekenstein Y, Kang J, Kley C S, Kim D, Gibson N A, Zhang D, Yu Y, Leone S R, Wang L W, Alivisatos A P, Yang P. Strongly quantum confined colloidal cesium tin iodide perovskite nanoplates: lessons for reducing defect density and improving stability. Nano Letters, 2018, 18(3): 2060–2066
6. Chen L J. Synthesis and optical properties of lead-free cesium germanium halide perovskite quantum rods. RSC Advances, 2018, 8(33): 18396–18399
7. Leng M, Yang Y, Zeng K, Chen Z, Tan Z, Li S, Li J, Xu B, Li D, Hautzinger M P, Fu Y, Zhai T, Xu L, Niu G, Jin S, Tang J. All-inorganic bismuth-based perovskite quantum dots with bright blue photoluminescence and excellent stability. Advanced Functional Materials, 2018, 28(1): 1704446
8. Luo J, Wang X, Li S, Liu J, Guo Y, Niu G, Yao L, Fu Y, Gao L, Dong Q, Zhao C, Leng M, Ma F, Liang W, Wang L, Jin S, Han J, Zhang L, Etheridge J, Wang J, Yan Y, Sargent E H, Tang J. Efficient and stable emission of warm-white light from lead-free halide double perovskites. Nature, 2018, 563(7732): 541–545
9. Li J, Wang H, Li D. Self-trapped excitons in two-dimensional perovskites. Frontiers of Optoelectronics, 2020, 13(3): 225–234
10. Li S, Luo J, Liu J, Tang J. Self-trapped excitons in all-inorganic halide perovskites: fundamentals, status, and potential applications. Journal of Physical Chemistry Letters, 2019, 10(8): 1999–2007
11. Smith M D, Karunadasa H I. White-light emission from layered halide perovskites. Accounts of Chemical Research, 2018, 51(3): 619–627
12. Jun T, Sim K, Iimura S, Sasase M, Kamioka H, Kim J, Hosono H. Lead-free highly efficient blue-emitting $Cs_3Cu_2I_5$ with 0D electronic structure. Advanced Materials, 2018, 30(43): e1804547
13. Creason T D, Yangui A, Roccanova R, Strom A, Du M H, Saparov B. Rb_2CuX_3 (X = Cl, Br): 1D all-inorganic copper halides with ultrabright blue emission and up-conversion photoluminescence. Advanced Optical Materials, 2020, 8(2): 1901338
14. Lin R, Guo Q, Zhu Q, Zhu Y, Zheng W, Huang F. All-inorganic $CsCu_2I_3$ single crystal with high-PLQY (≈15.7%) intrinsic white-light emission via strongly localized 1D excitonic recombination. Advanced Materials, 2019, 31(46): e1905079
15. Roccanova R, Yangui A, Nhalil H, Shi H, Du M H, Saparov B. Near-unity photoluminescence quantum yield in blue-emitting $Cs_3Cu_2Br_{5-x}I_x$ ($0 \leqslant x \leqslant 5$). ACS Applied Electronic Materials, 2019, 1(3): 269–274
16. Creason T D, McWhorter T M, Bell Z, Du M H, Saparov B. K_2CuX_3 (X = Cl, Br): all-inorganic lead-free blue emitters with near-unity photoluminescence quantum yield. Chemistry of Materials, 2020, 32(14): 6197–6205
17. Luo Z, Li Q, Zhang L, Wu X, Tan L, Zou C, Liu Y, Quan Z. 0D $Cs_3Cu_2X_5$ (X = I, Br, and Cl) nanocrystals: colloidal syntheses and optical properties. Small, 2020, 16(3): e1905226
18. Sebastia-Luna P, Navarro-Alapont J, Sessolo M, Palazon F, Bolink H J. Solvent-free synthesis and thin-film deposition of cesium copper halides with bright blue photoluminescence. Chemistry of Materials, 2019, 31(24): 10205–10210
19. Roccanova R, Yangui A, Seo G, Creason T D, Wu Y, Kim D Y, Du M H, Saparov B. Bright luminescence from nontoxic $CsCu_2X_3$ (X = Cl, Br, I). ACS Materials Letters, 2019, 1(4): 459–465
20. Yang B, Yin L, Niu G, Yuan J H, Xue K H, Tan Z, Miao X S, Niu M, Du X, Song H, Lifshitz E, Tang J. Lead-free halide Rb_2CuBr_3 as sensitive X-ray scintillator. Advanced Materials, 2019, 31(44): e1904711
21. Li J, Inoshita T, Ying T, Ooishi A, Kim J, Hosono H. A highly efficient and stable blue-emitting $Cs_5Cu_3Cl_6I_2$ with a 1D chain structure. Advanced Materials, 2020, 32(37): e2002945
22. Li Q, Chen Z, Yang B, Tan L, Xu B, Han J, Zhao Y, Tang J, Quan Z. Pressure-induced remarkable enhancement of self-trapped exciton emission in one-dimensional $CsCu_2I_3$ with tetrahedral units. Journal of the American Chemical Society, 2020, 142(4): 1786–1791
23. Li Y, Shi Z, Wang L, Chen Y, Liang W, Wu D, Li X, Zhang Y, Shan C, Fang X. Solution-processed one-dimensional $CsCu_2I_3$ nanowires for polarization-sensitive and flexible ultraviolet photodetectors. Materials Horizons, 2020, 7(6): 1613–1622
24. Guo Z, Li J, Gao Y, Cheng J, Zhang W, Pan R, Chen R, He T. Multiphoton absorption in low-dimensional cesium copper iodide single crystals. Journal of Materials Chemistry C, Materials for Optical and Electronic Devices, 2020, 8(47): 16923–16929
25. Grandhi G K, Viswanath N S M, Cho H B, Han J H, Kim S M, Choi S, Im W B. Mechanochemistry as a green route: synthesis, thermal stability, and postsynthetic reversible phase transformation of highly-luminescent cesium copper halides. Journal of Physical Chemistry Letters, 2020, 11(18): 7723–7729
26. Lian L, Zheng M, Zhang P, Zheng Z, Du K, Lei W, Gao J, Niu G, Zhang D, Zhai T, Jin S, Tang J, Zhang X, Zhang J. Photophysics in $Cs_3Cu_2X_5$ (X = Cl, Br, or I): highly luminescent self-trapped excitons from local structure symmetrization. Chemistry of Materials, 2020, 32(8): 3462–3468
27. Cheng P, Sun L, Feng L, Yang S, Yang Y, Zheng D, Zhao Y, Sang

Y, Zhang R, Wei D, Deng W, Han K. Colloidal synthesis and optical properties of all-inorganic low-dimensional cesium copper halide nanocrystals. Angewandte Chemie International Edition, 2019, 58 (45): 16087–16091

28. Vashishtha P, Nutan G V, E. Griffith B, Fang Y, Giovanni D, Jagadeeswararao M, Sum T C, Mathews N, Mhaisalkar S G, Hanna J V, White T. Cesium copper iodide tailored nanoplates and nanorods for blue, yellow, and white emission. Chemistry of Materials, 2019, 31(21): 9003–9011
29. Liu S, Yue Y, Zhang X, Wang C, Yang G, Zhu D. A controllable and reversible phase transformation between all-inorganic perovskites for white light emitting diodes. Journal of Materials Chemistry C, Materials for Optical and Electronic Devices, 2020, 8(25): 8374–8379
30. Williams R T, Song K S. The self-trapped exciton. Journal of Physics and Chemistry of Solids, 1990, 51(7): 679–716
31. Yang J, Kang W, Liu Z, Pi M, Luo L B, Li C, Lin H, Luo Z, Du J, Zhou M, Tang X. High-performance deep ultraviolet photodetector based on a one-dimensional lead-free halide perovskite $CsCu_2I_3$ film with high stability. Journal of Physical Chemistry Letters, 2020, 11 (16): 6880–6886
32. Ma Z, Liu Z, Lu S, Wang L, Feng X, Yang D, Wang K, Xiao G, Zhang L, Redfern S A T, Zou B. Pressure-induced emission of cesium lead halide perovskite nanocrystals. Nature Communications, 2018, 9(1): 4506
33. Shi Y, Ma Z, Zhao D, Chen Y, Cao Y, Wang K, Xiao G, Zou B. Pressure-induced emission (PIE) of one-dimensional organic tin bromide perovskites. Journal of the American Chemical Society, 2019, 141(16): 6504–6508
34. Wang Y, Lü X, Yang W, Wen T, Yang L, Ren X, Wang L, Lin Z, Zhao Y. Pressure-induced phase transformation, reversible amorphization, and anomalous visible light response in organolead bromide perovskite. Journal of the American Chemical Society, 2015, 137(34): 11144–11149
35. Du M H. Emission trend of multiple self-trapped excitons in luminescent 1D copper halides. ACS Energy Letters, 2020, 5(2): 464–469
36. Kentsch R, Morgenroth M, Scholz M, Xu K, Schmedt Auf der Günne J, Lenzer T, Oum K. Direct observation of the exciton self-trapping process in $CsCu_2I_3$ thin films. Journal of Physical Chemistry Letters, 2020, 11(11): 4286–4291
37. Fang S, Wang Y, Li H, Fang F, Jiang K, Liu Z, Li H, Shi Y. Rapid synthesis and mechanochemical reactions of cesium copper halides for convenient chromaticity tuning and efficient white light emission. Journal of Materials Chemistry. C, Materials for Optical and Electronic Devices, 2020, 8(14): 4895–4901
38. Ma Z, Shi Z, Qin C, Cui M, Yang D, Wang X, Wang L, Ji X, Chen X, Sun J, Wu D, Zhang Y, Li X J, Zhang L, Shan C. Stable yellow light-emitting devices based on ternary copper halides with broadband emissive self-trapped excitons. ACS Nano, 2020, 14 (4): 4475–4486
39. Wang L, Shi Z, Ma Z, Yang D, Zhang F, Ji X, Wang M, Chen X, Na G, Chen S, Wu D, Zhang Y, Li X, Zhang L, Shan C. Colloidal synthesis of ternary copper halide nanocrystals for high-efficiency deep-blue light-emitting diodes with a half-lifetime above 100 h. Nano Letters, 2020, 20(5): 3568–3576
40. Ma Z, Shi Z, Yang D, Li Y, Zhang F, Wang L, Chen X, Wu D, Tian Y, Zhang Y, Zhang L, Li X, Shan C. High color-rendering index and stable white light-emitting diodes by assembling two broadband emissive self-trapped excitons. Advanced Materials, 2021, 33(2): e2001367
41. Lin R, Zhu Q, Guo Q, Zhu Y, Zheng W, Huang F. Dual self-trapped exciton emission with ultrahigh photoluminescence quantum yield in $CsCu_2I_3$ and $Cs_3Cu_2I_5$ perovskite single crystals. Journal of Physical Chemistry C, 2020, 124(37): 20469–20476
42. Li Y, Shi Z, Liang W, Wang L, Li S, Zhang F, Ma Z, Wang Y, Tian Y, Wu D, Li X, Zhang Y, Shan C, Fang X. Highly stable and spectrum-selective ultraviolet photodetectors based on lead-free copper-based perovskites. Materials Horizons, 2020, 7(2): 530–540
43. Zhang Z X, Li C, Lu Y, Tong X W, Liang F X, Zhao X Y, Wu D, Xie C, Luo L B. Sensitive deep ultraviolet photodetector and image sensor composed of inorganic lead-free $Cs_3Cu_2I_5$ perovskite with wide bandgap. Journal of Physical Chemistry Letters, 2019, 10(18): 5343–5350
44. Li Z, Li Z, Shi Z, Fang X. Facet-dependent, fast response, and broadband photodetector based on highly stable all-inorganic $CsCu_2I_3$ single crystal with 1d electronic structure. Advanced Functional Materials, 2020, 30(28): 2002634
45. Zhao X, Niu G, Zhu J, Yang B, Yuan J H, Li S, Gao W, Hu Q, Yin L, Xue K H, Lifshitz E, Miao X, Tang J. All-inorganic copper halide as a stable and self-absorption-free X-ray scintillator. Journal of Physical Chemistry Letters, 2020, 11(5): 1873–1880
46. Gao W, Niu G, Yin L, Yang B, Yuan J H, Zhang D, Xue K H, Miao X, Hu Q, Du X, Tang J. One-dimensional all-inorganic K_2CuBr_3 with violet emission as efficient X-ray scintillators. ACS Applied Electronic Materials, 2020, 2(7): 2242–2249
47. Lian L, Zheng M, Zhang W, Yin L, Du X, Zhang P, Zhang X, Gao J, Zhang D, Gao L, Niu G, Song H, Chen R, Lan X, Tang J, Zhang J. Efficient and reabsorption-free radioluminescence in $Cs_3Cu_2I_5$ nanocrystals with self-trapped excitons. Advanced Science, 2020, 7(11): 2000195
48. Zhang F, Zhao Z, Chen B, Zheng H, Huang L, Liu Y, Wang Y, Rogach A L. Strongly emissive lead-free 0D $Cs_3Cu_2I_5$ perovskites synthesized by a room temperature solvent evaporation crystallization for down-conversion light-emitting devices and fluorescent inks. Advanced Optical Materials, 2020, 8(8): 1901723
49. Zeng F, Guo Y, Hu W, Tan Y, Zhang X, Feng J, Tang X. Opportunity of the lead-free all-inorganic $Cs_3Cu_2I_5$ perovskite film for memristor and neuromorphic computing applications. ACS Applied Materials & Interfaces, 2020, 12(20): 23094–23101

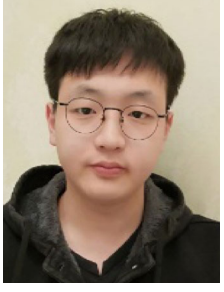

Boyu Zhang is currently a postgraduate student of the Hubei Key Laboratory of Low Dimensional Optoelectronic Materials and Devices, Hubei University of Arts and Science, China. His research interests are focused on optoelectronic materials and ultrafast spectroscopy.

Xian Wu is currently a postgraduate student of the Hubei Key Laboratory of Low Dimensional Optoelectronic Materials and Devices, Hubei University of Arts and Science, China. His research interests are focused on the optoelectronic materials and ultrafast spectroscopy.

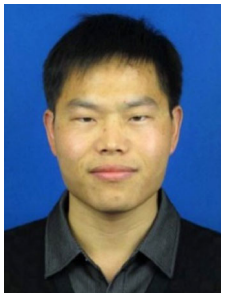

Shuxing Zhou is currently a lecturer of Hubei University of Arts and Science, China. He received his Ph.D. degree in Electronics from Shanghai Institute of Microsystem and Information Technology, Chinese Academy of Sciences, China in 2016. His current research interests are focused on the electronic material devices and their reliability.

Guijie Liang is currently a professor and vice-director of the Hubei Key Laboratory of Low Dimensional Optoelectronic Materials and Devices, Hubei University of Arts and Science, China. He obtained his Ph.D. degree from the Department of Materials, Xi'an Jiaotong University, China in 2011. His current research interests include low dimensional optoelectronic materials and ultrafast spectroscopy.

Qingsong Hu received his Ph.D. degree in Chemistry and Material from Zhejiang University of Technology, China in 2016. He then completed his post-doctoral research at Huazhong University of Science and Technology, China from 2016 to 2020. He is currently an associate professor of Hubei University of Arts and Science, China. His research interests are focused on the novel luminescent material, phenomena, and mechanism.